Strong evidence for a weakly oxygenated ocean–atmosphere system during the Proterozoic

Changle Wang[a,b,c,1,2], Maxwell A. Lechte[d,1,2], Christopher T. Reinhard[e], Dan Asael[b], Devon B. Cole[e], Galen P. Halverson[d], Susannah M. Porter[f], Nir Galili[g], Itay Halevy[g], Robert H. Rainbird[h], Timothy W. Lyons[i], and Noah J. Planavsky[b]

[a]Key Laboratory of Mineral Resources, Institute of Geology and Geophysics, Chinese Academy of Sciences, Beijing 100029, China; [b]Department of Geology and Geophysics, Yale University, New Haven, CT 06511; [c]College of Earth and Planetary Sciences, University of Chinese Academy of Sciences, Beijing 100049, China; [d]Department of Earth and Planetary Sciences, McGill University, Montréal, QC H3A 0E8, Canada; [e]School of Earth and Atmospheric Sciences, Georgia Institute of Technology, Atlanta, GA 30318; [f]Department of Earth Science, University of California, Santa Barbara, CA 93106; [g]Department of Earth and Planetary Sciences, Weizmann Institute of Science, Rehovot 761001, Israel; [h]Geological Survey of Canada, Ottawa, ON K1A 0E8, Canada; and [i]Department of Earth Sciences, University of California, Riverside, CA 92521

Edited by Mark Thiemens, Department of Chemistry and Biochemistry, University of California San Diego, La Jolla, CA; received September 11, 2021; accepted December 16, 2021

Earth's surface has undergone a protracted oxygenation, which is commonly assumed to have profoundly affected the biosphere. However, basic aspects of this history are still debated—foremost oxygen (O_2) levels in the oceans and atmosphere during the billion years leading up to the rise of algae and animals. Here we use isotope ratios of iron (Fe) in ironstones—Fe-rich sedimentary rocks deposited in nearshore marine settings—as a proxy for O_2 levels in shallow seawater. We show that partial oxidation of dissolved Fe(II) was characteristic of Proterozoic shallow marine environments, whereas younger ironstones formed via complete oxidation of Fe(II). Regardless of the Fe(II) source, partial Fe(II) oxidation requires low O_2 in the shallow oceans, settings crucial to eukaryotic evolution. Low O_2 in surface waters can be linked to markedly low atmospheric O_2—likely requiring less than 1% of modern levels. Based on our records, these conditions persisted (at least periodically) until a shift toward higher surface O_2 levels between *ca.* 900 and 750 Ma, coincident with an apparent rise in eukaryotic ecosystem complexity. This supports the case that a first-order shift in surface O_2 levels during this interval may have selected for life modes adapted to more oxygenated habitats.

ironstone | isotopes | iron | oxygenation | Proterozoic

It is widely accepted that atmospheric oxygen (O_2) first accumulated to appreciable levels early in the Proterozoic Eon (2500 to 541 Ma), over a time interval known as the Great Oxidation Event (1, 2). A subsequent stepwise increase in atmospheric O_2 has been hypothesized to have paved the way for the emergence of animal life at some point in the late Proterozoic (3). However, the atmospheric O_2 levels (pO_2) of the ocean–atmosphere system during Earth's intervening history (i.e., the middle Proterozoic) are highly debated: Despite suggestions that pO_2 remained relatively low during this time (4–6), recent work has argued that the O_2 demands of complex eukaryotes may have been exceeded well before their evolution (e.g., refs. 7–10). Therefore, the nature of the relationships between surface oxygenation and the evolutionary ecology of early complex life remain contentious (8, 11). Because surface redox conditions can affect the geochemistry of contemporaneous sediments, several geochemical indices from ancient sedimentary rocks have been employed as proxies for mid-Proterozoic atmospheric pO_2, predominantly the abundance or isotopic composition of redox-sensitive trace metals in marine carbonate rocks or shales (e.g., refs. 2, 6, 9, 10, 12). Atmospheric pO_2 estimates from these proxies are often characterized by large uncertainties, suffer from apparently conflicting inferred pO_2 histories, or both. A robust, mechanistically understood and sensitive proxy for mid-Proterozoic O_2 levels is therefore required.

Iron (Fe) in seawater is soluble under anoxic conditions [as Fe(II)] and poorly soluble under oxic conditions [precipitating as Fe(III) oxyhydroxides]. Although oxidation of Fe(II) can also occur under anoxic conditions (via photo-oxidation or anoxygenic photosynthesis; ref. 13), the rate and extent of Fe(II) oxidation in aqueous environments—either abiotic or biologically mediated—will depend greatly on the abundance of O_2. Therefore, secular records of marine Fe(II) oxidation can potentially be used to track O_2 levels in seawater. At the low surface O_2 levels characteristic of early Earth, marine Fe(II) availability would have been comparatively high (sourced from hydrothermal inputs and the redox cycling of continental Fe), and partial oxidation of this seawater Fe(II) reservoir would have been common (14, 15). At higher O_2 levels characteristic of the modern oceans and atmosphere, any Fe(II) inputs to surface waters are quantitatively oxidized (16).

Based upon the kinetics of Fe(II) oxidation and the associated Fe isotope systematics (16–18), it is possible to estimate the abundance of O_2 in seawater based upon the Fe isotope

Significance

Earth's transition from anoxic oceans and atmosphere to a well-oxygenated state led to major changes in nearly every surficial system. However, estimates of surface oxygen levels in the billion years preceding this shift span two orders of magnitude, suggesting a poor understanding of the evolution of the oxygen cycle. We use the isotopic record of iron oxides deposited in ancient shallow marine environments to show that oxygen remained at extremely low levels in the ocean–atmosphere system for most of Earth's history, and that a rise in oxygen occurred in step with the expansion of complex, eukaryotic ecosystems. These results indicate that Earth is capable of stabilizing at low atmospheric oxygen levels, with important implications for exploration of exoplanet biosignatures.

Author contributions: C.W., M.A.L., and N.J.P. designed research; C.W., M.A.L., C.T.R., D.A., D.B.C., G.P.H., S.M.P., N.G., I.H., R.H.R., T.W.L., and N.J.P. performed research; M.A.L., C.T.R., D.A., D.B.C., G.P.H., S.M.P., N.G., I.H., R.H.R., T.W.L., and N.J.P. contributed new reagents/analytic tools; C.W., M.A.L., C.T.R., D.A., D.B.C., G.P.H., S.M.P., N.G., I.H., R.H.R., T.W.L., and N.J.P. analyzed data; and C.W., M.A.L., and N.J.P. wrote the paper.

The authors declare no competing interest.

This article is a PNAS Direct Submission.

[1]C.W. and M.A.L. contributed equally to this work.

[2]To whom correspondence may be addressed. Email: wangcl@mail.iggcas.ac.cn or maxwell.lechte@mail.mcgill.ca.

This article contains supporting information online at http://www.pnas.org/lookup/suppl/doi:10.1073/pnas.2116101119/-/DCSupplemental.

Published January 31, 2022.

composition of chemical sediments (14). The partial oxidation of dissolved Fe(II) can lead to equilibrium fractionation whereby the produced Fe(III) (oxyhydr)oxides are enriched in ^{56}Fe by up to 1.0 to 3.2‰ (reported as the ratio of ^{56}Fe/^{54}Fe relative to the IRMM-014 standard reference material in parts per thousand; δ^{56}Fe) (17, 18). More rapid oxidation effectively lowers this overall fractionation (14, 18), and quantitative oxidation produces Fe(III) oxyhydroxides with an Fe isotope composition that mirrors that of the Fe(II) source. Biologically mediated Fe(II) oxidation (facilitated by anoxygenic phototrophs under anoxic conditions or microaerophilic chemotrophs under suboxic conditions) results in similar Fe isotope fractionations to that of abiotic Fe(II) oxidation (18) (*SI Appendix*). Compared to paleoredox proxies based on trace element geochemistry, the Fe isotopic composition of Fe-rich chemical sedimentary rocks is expected to be strongly rock-buffered, less likely to be affected by detrital contamination, and resistant to postdepositional alteration. Therefore, Fe-rich rocks can serve as robust Fe isotope archives in deep time (14, 18, 19) and can be used to constrain the redox state of ancient seawater.

The Ironstone Record of Shallow Marine Redox Conditions

The Proterozoic oceans were likely to have been characterized by a strong redox depth gradient, with anoxic and Fe(II)-bearing (ferruginous) deep oceans overlain by O_2-bearing surface waters in contact with an oxygenated atmosphere, with anoxic and H_2S-bearing (euxinic) zones variably developed at mid-depths along productive continental margins (2). Constraining the O_2 concentrations ($[O_2]$) of this oxygenated surface layer is essential to understanding the evolution of early aerobic eukaryotes. Iron isotope studies of Fe-rich sedimentary rocks can offer important insights into ancient marine redox conditions. However, most of these studies have focused on banded iron formations, which are generally interpreted to have been deposited in deeper (below wave base) marine settings that are potentially less directly coupled with the atmosphere (20).

The term "ironstone" is used to describe noncherty, sand- and clay-rich rock units with >15 wt % Fe that feature ooids with cortical laminae composed of either Fe(III) oxides (goethite or hematite) or Fe(II) silicates (berthierine or chamosite) (21). The sedimentology of ironstones indicates formation at the sediment–seawater interface, such as Fe ooids infilling the interstices of stromatolites (19), fossils of encrusting marine organisms within Fe ooid cortices (22), and reworked Fe ooid fragments forming composite nuclei (Fig. 1 and *SI Appendix*). Importantly, based on sedimentary facies associations, ironstones are widely accepted to have formed in shallow (peritidal, estuarine, lagoonal, and storm-influenced) marine environments (21). Ironstones are common in the Phanerozoic stratigraphic record, and some deposits that fit the definition and classic depositional settings of ironstones are reported from the Proterozoic (e.g., refs. 19 and 23). Several Proterozoic deposits described as granular iron formations fall into this category, featuring sedimentary evidence for deposition above storm wave base and containing Fe ooids (20, 24). For simplicity, herein we collectively refer to all of these shallow-marine, commonly Fe ooid-bearing, Fe-rich deposits as ironstones. These ironstones offer a unique window into shallow marine settings pertinent to Proterozoic eukaryotic ecosystems.

To gain insights into the O_2 levels of mid-Proterozoic shallow seawater we analyzed the Fe isotope compositions (n = 150) of Proterozoic ironstones from seven different localities, which collectively span *ca*. 1,880 to 750 Ma (Fig. 1, *SI Appendix*, Fig. S5, and Dataset S1), supplemented by additional data from the published literature (19, 24, 25) (n = 60; *SI Appendix*). These targeted ironstones are all predominantly composed of Fe(III) oxides (hematite) and lack Fe(II) sulfides (e.g., pyrite), with some ironstones featuring subordinate Fe(II) silicates (berthierine/chamosite; see *SI Appendix*). The depositional basins of these Proterozoic ironstones are interpreted to have been anoxic and ferruginous below an oxygenated surface layer in contact with the atmosphere, with no clear evidence for contemporaneous local euxinia (19, 23, 24) (*SI Appendix*). We compare these Proterozoic Fe isotope results to data (n = 51) from 10 Phanerozoic ironstones and Holocene ferruginous shallow marine sediments that formed under a well-oxygenated ocean–atmosphere system.

Ironstone Iron Isotope Compositions

Ironstones comprise authigenic precipitates that require an abundant supply of mobile Fe(II) for their genesis, which can be supplied by anoxic seawater enriched in Fe(II) from distal hydrothermal sources (19, 21, 26) or a benthic Fe(II) flux sourced from the reduction of continentally sourced Fe(III) (e.g., ref. 27). The Fe isotope composition of hydrothermal Fe(II) and igneous rocks covers a limited range around 0‰ (typically $-0.5 < \delta^{56}\text{Fe} < 0.3$‰), whereas Fe(II) sourced from Fe(III) reduction is generally characterized by negative δ^{56}Fe values (18, 28). Fractionation beyond these input values can therefore implicate genetic processes. The studied Phanerozoic ironstones and Holocene ferruginous sediments display a narrow range of isotopic compositions ($-0.4 \leq \delta^{56}\text{Fe} \leq 0.3$‰), which are indistinguishable from those of hydrothermal and igneous Fe(II) sources (Fig. 2). The results show a statistically significant difference between the Proterozoic and Phanerozoic ironstones. In contrast to the younger equivalents, nearly all of the studied Proterozoic ironstones have highly variable and mostly positive δ^{56}Fe values (Fig. 2). The exception to this rule is the youngest of the Proterozoic ironstones in our dataset—the *ca*. 750 Ma Galeros Formation in Arizona—which displays a notably limited range in δ^{56}Fe values (Fig. 2) that are not statistically different from those of Phanerozoic ironstones.

An Isotopic Fingerprint of Marine Partial Fe(II) Oxidation

The Fe isotopic composition of Fe(III) oxide-bearing sediments is determined by several factors, including the Fe(II) source, the rates of Fe(II) supply and oxidation, and the relative proportion of authigenic Fe(III) (oxyhydr)oxides compared to the total Fe contents. In well-oxygenated surface waters, the oxidation of seawater Fe(II) goes to completion, resulting in a narrow range in δ^{56}Fe values that reflects that of the Fe(II) source (likely close to 0‰) (16, 17). The much greater spread in Fe isotope compositions in the Proterozoic ironstones (relative to the Phanerozoic ironstones), including positive and negative δ^{56}Fe values, is best explained by distillation processes involving partial Fe(II) oxidation.

Although negative δ^{56}Fe values in ironstones could indicate that the local seawater was enriched in isotopically light Fe(II) produced via dissimilatory Fe(III) reduction (17, 18, 28), this

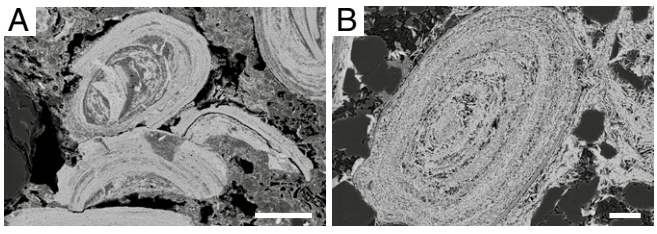

Fig. 1. Back-scattered electron images of Proterozoic ironstones. (*A*) Composite hematitic ooid with nuclei composed of ooid fragments in the *ca*. 1,880 Ma Gibralter Formation, indicating ooid reworking during ironstone genesis. (*B*) Hematitic ooid and hematite-cemented quartz sand in the *ca*. 750 Ma Galeros Formation. (Scale bars, 100 μm.)

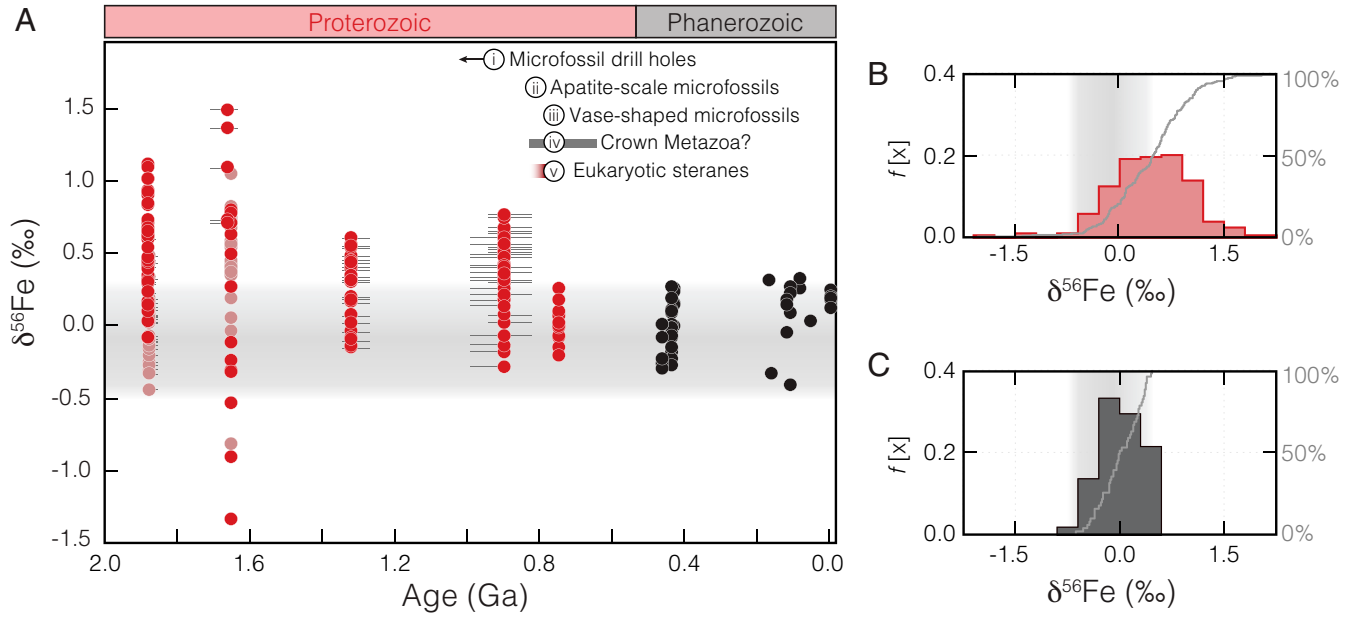

Fig. 2. Variation in δ^{56}Fe values of ironstones through geological time. (*A*) Bulk-rock δ^{56}Fe data shown for Proterozoic ironstones (filled red circles are from this study; faded red filled circles are from previously published data) and Phanerozoic ironstones and Fe-rich sediments (filled black circles). Sample SE is smaller than the data points, and horizontal error bars denote the permissible range of age estimates for the ironstones. Estimates for the timing of several evolutionary advancements are indicated, including fossil evidence for eukaryotic predation [based upon 1) microfossil drill holes (67); 2) apatite-scale microfossils (64); and 3) vase-shaped microfossils (63)]; 4) molecular clock estimates for the divergence of crown-group metazoans (65); and 5) the first appearance of abundant eukaryotic steranes in the biomarker record (59). Relative frequency histograms and cumulative frequency distributions of Proterozoic (*B*) and Phanerozoic (*C*) data are also shown. Horizontal and vertical gray fields denote the range of δ^{56}Fe values of the igneous and hydrothermal Fe(II) sources ($-0.5 < \delta^{56}\text{Fe} < 0.3$‰) (18).

signature could also result from the ongoing removal of isotopically heavy Fe via the progressive partial oxidation of a seawater Fe(II) reservoir (i.e., isotopic distillation) (15, 18). When Fe(II) oxidation is extensive, the δ^{56}Fe values of the resultant Fe(III) (oxyhydr)oxides can follow a predictable distribution that is weighted toward higher δ^{56}Fe values (approximating the instantaneous product of Fe(II) oxidation; *SI Appendix*), with a gradual trend of decreasing relative frequency toward lower δ^{56}Fe values. This trend is most clearly evident in the data from the *ca*. 1,650 Ma Chuanlinggou Formation ironstone (North China), for which δ^{56}Fe values are most commonly between 0.6 and 1.0‰, with more negative values becoming progressively less common (Fig. 3*A*). Assuming an initial seawater Fe(II) with δ^{56}Fe values close to 0‰, this may suggest an instantaneous fractionation of ~0.8‰ associated with Fe(II) oxidation and the precipitation of ironstone Fe(III) (oxyhydr)oxides in the low O_2 Proterozoic surface waters. The interpretation that the Fe isotope signature of the Chuanlinggou ironstone is controlled by partial oxidation is strongly supported by a negative correlation between δ^{56}Fe values and Mn enrichment (Mn/Fe ratios; Fig. 3*B*, which are typically considered a proxy for marine oxidation (29).

Most of the other Proterozoic ironstones do not show this full distribution ranging from positive to negative δ^{56}Fe values and generally show a spread in δ^{56}Fe values from ~0 to 1‰ (Fig. 2). This may suggest that Fe(II) oxidation in the waters sourcing these ironstones was not as extensive during their formation (Fig. 3). Local and regional variation in the δ^{56}Fe values of individual ironstone samples is an expected consequence when partial oxidation dominates, as there can be temporal and spatial variability in the extent of oxidation of different ferruginous water masses. Under a low pO_2 atmosphere, $[O_2]$ in shallow seawater can be locally elevated due to local primary production (30) but is unlikely to be depleted relative to gas-exchange equilibrium with the overlying atmosphere (*SI Appendix*, Fig. S2). Further, upwelling rates and initial dissolved Fe(II) concentrations can be variable, leading to different extents of Fe(II) oxidation at low O_2 levels. The spread in the isotopic composition of these ironstones (including negative and positive δ^{56}Fe values) is consistent with partial oxidation of an Fe(II) source with δ^{56}Fe values close to 0‰ (18).

These Fe isotope trends are suggestive of a high dissolved Fe(II):O_2 ratio of the contemporaneous shallow seawater. However, in order to attempt to leverage these Fe isotope data to obtain estimates for surface O_2 levels, it is important to consider other possible influences on the ironstone Fe isotope signatures such as variation in the isotopic composition of the Fe(II) source. In modern, oxic river waters and surface seawater, the stabilization in solution of otherwise highly insoluble Fe(III) by complexation with organic ligands can lead to dissolved Fe(III) with positive δ^{56}Fe values (e.g., refs. 31 and 32). However, this process has not been shown to result in isotopically heavy Fe in the marginal sediments (31, 33), and the bulk isotopic composition of Fe in rivers and estuarine sediments is typically close to (or slightly lighter than) average crustal values (31, 34). Given that organic ligands stabilize Fe(III) in solution, we suggest that ligand-bound Fe(III) did not play a major role in the formation of ironstones.

Kinetic isotope effects during the precipitation of Fe(II) sulfides from dissolved Fe(II) can involve negative fractionation, and this is expressed most strongly during partial pyrite formation when H_2S availability is limited (35). Iron isotopic fractionation related to pyrite formation has been shown to be an important process in modern euxinic basins and may have been active in localized euxinic water masses during the Proterozoic (36). However, the possible effects of this process on the isotopic composition of marine Fe(II) would have depended upon the relative availability of Fe(II) and H_2S in the mid-depth euxinic zone, where developed. If ferruginous seawater interacted with euxinic water masses in the middle Proterozoic, H_2S

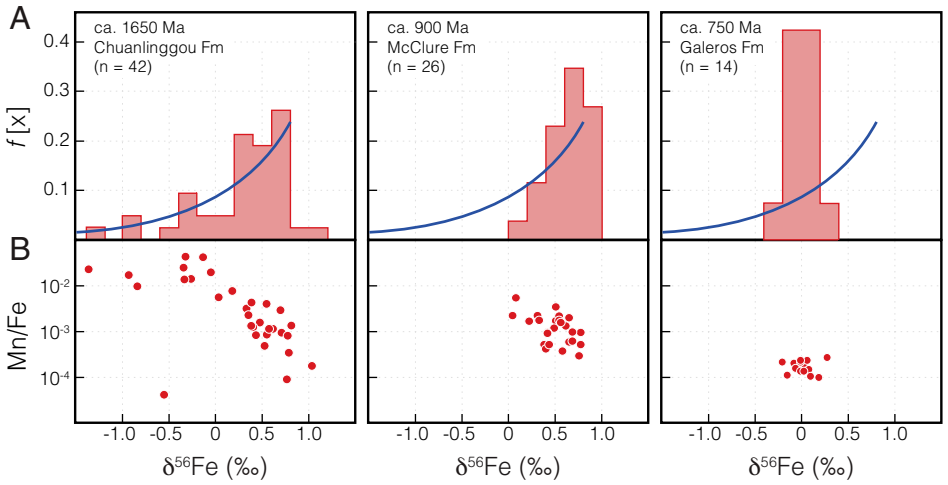

Fig. 3. Iron isotope trends of selected Proterozoic ironstones. (*A*) Relative frequency histogram of δ^{56}Fe values. For the Chuanlinggou ironstone, these values show a cluster around 0.8‰ with gradually decreasing relative frequency toward more negative values. For comparison, the dark blue line represents the δ^{56}Fe distribution predicted for Fe(III) (oxyhydr)oxides produced by progressive oxidation according to Rayleigh distillation processes (e.g., ref. 68), assuming an initial Fe(II) source with δ^{56}Fe = 0‰ and an instantaneous fractionation of 0.8‰ for the combined processes of Fe(II) oxidation and precipitation as Fe(III) (oxyhydr)oxides. For the McClure ironstone, δ^{56}Fe values show a similar cluster around 0.8‰, but the tail of the distribution toward lower δ^{56}Fe values is not as well-developed. For the Galeros ironstone, δ^{56}Fe values cluster around 0‰ with a narrow range, interpreted to indicate quantitative oxidation of an unfractionated Fe(II) source. (*B*) Cross-plot diagram showing the relationship between Mn enrichment (Mn/Fe) versus δ^{56}Fe values, a proxy for degree of oxidation. For the Chuanlinggou ironstone, these data show that more negative δ^{56}Fe values are typically Mn-enriched and likely indicate a greater degree of water column oxidation. This trend is also less developed for the McClure ironstone, which lacks negative δ^{56}Fe values, and is absent in the Galeros ironstone.

would likely have been in excess and seawater Fe(II) would have been depleted due to quantitative pyrite formation, producing sedimentary pyrite that largely matches the δ^{56}Fe values of the original Fe(II) source (36). In this scenario, isotopically heavy Fe(II) is not supplied to shallow waters due to quantitative drawdown near the redoxcline, and therefore this process would not affect the isotopic composition of nearshore sediments. These Fe–S systematics are demonstrated by data from modern euxinic basins where sedimentary pyrite is not strongly fractionated (28) and seawater Fe(II) near or above the redoxcline is not ^{56}Fe-enriched (36).

For sedimentary pyrite deposited after the Great Oxidation Event, δ^{56}Fe values are typically unfractionated or positive (15, 17) (*SI Appendix*, Fig. S7). This may suggest that fractionation and isotopic distillation due to partial pyrite formation was not an important process in the middle Proterozoic (*SI Appendix*). More data from this interval are needed, and investigations into the triple Fe isotope composition of Proterozoic Fe(II) sulfides and Fe(III) oxides may help to better elucidate the importance of the sulfide Fe sink during this time (37). In sum, the sedimentary Fe record is more consistent with a partial oxidation control on ironstone Fe isotope fractionation, rather than the quantitative drawdown of a fractionated Fe(II) source. Proterozoic ironstones feature a spread in δ^{56}Fe values (including negative values) (Fig. 2), whereas quantitative oxidation of isotopically heavy Fe(II) would predict a narrow range clustered around the value of the Fe(II) source. Further, trends in the δ^{56}Fe data and Mn/Fe ratios of the Chuanlinggou Formation are similar to those predicted by Rayleigh-like isotopic distillation due to partial Fe(II) (Fig. 3); these are also difficult to reconcile with fractionation due to light Fe removal and are strong evidence for an oxidative control on the ironstone Fe isotope composition.

Postdepositional processes can also affect the Fe isotopic composition of marine sediments. The microbial reduction of Fe(III) coupled to organic matter oxidation can preferentially release light Fe isotopes to solution (18, 28). Even under anoxic conditions, however, this process only results in a negligible effect on the bulk Fe isotopic composition of shelf sediments (16, 33), because only a fraction of sedimentary Fe(III) is bioavailable and Fe(III) reduction is limited by the availability of organic matter. This isotopic effect of benthic Fe(II) loss is observed in shelf sediments with much lower Fe contents (typically <4 wt %) than ironstones (33), and our studied samples are rich in Fe(III) oxides with low organic matter which would strongly buffer against substantial Fe leaching during diagenesis or alteration. Authigenic Fe(II)-bearing minerals [such as the Fe(II) clays berthierine or chamosite] are present in some of the studied ironstones, yet the formation of Fe(II)-bearing phases generally produces minerals that are either unfractionated or isotopically light relative to the initial aqueous Fe(II) (18). Because Fe mobility is low under oxidizing conditions, postdepositional oxidation of these phases is unlikely to alter their primary Fe isotopic signature. Therefore, authigenic Fe(II) clays may contribute to the data spread but cannot explain the positive δ^{56}Fe values, which likely represent a primary signal. Kinetic isotope effects during Fe(II) sulfide authigenesis can result in a wide range in δ^{56}Fe values (*SI Appendix*, Fig. S7), yet all of the studied ironstones lack evidence for oxidized Fe(II) sulfide precursor phases (*SI Appendix*). In sum, regardless of whether Fe(II) was supplied by upwelling seawater or local Fe cycling, the positive δ^{56}Fe values in our data can only be explained by the partial oxidation of Fe(II) due to a high Fe(II):O_2 ratio (e.g., refs. 14, 17, 18).

Low Surface O_2 during the Middle Proterozoic

In modern redox-stratified lakes with anoxic and Fe(II)-rich bottom waters, considered an analog for the low-O_2 oceans of the early Earth, surface waters are oxygenated due to gas exchange with the atmosphere. In these settings, upwelling Fe(II) from the ferruginous water column is completely and rapidly oxidized, and the resultant Fe(III) oxyhydroxides are isotopically unfractionated relative to the dissolved Fe(II) pool (16). Therefore, partial Fe(II) oxidation in the upper water column requires lower [O_2] than present levels. By combining our Fe isotope data with a model for Fe(II) oxidation kinetics, we can use ironstones to estimate the ancient shallow seawater [O_2].

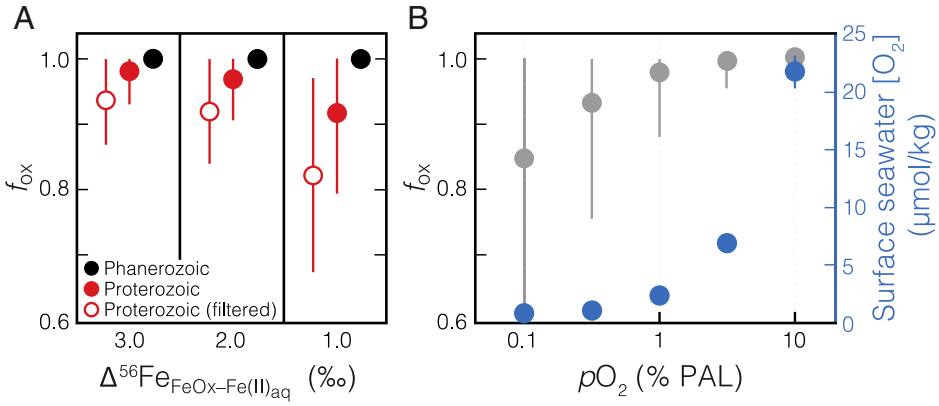

Fig. 4. A model for Fe(II) oxidation in Proterozoic and Phanerozoic ironstones as a function of atmospheric pO_2. (*A*) Using a Rayleigh distillation model, the fraction of the shallow seawater Fe(II) reservoir oxidized (f_{ox}) can be estimated based upon each ironstone Fe isotope value (i.e., more positive δ^{56}Fe values indicate a lesser extent of oxidation; *SI Appendix*). Assuming three different scenarios for the overall isotope fractionation effect of the combined processes of Fe(II) oxidation and precipitation as Fe(III) (oxyhydr)oxides ($\Delta^{56}Fe_{FeOx-Fe(II)aq}$ = 1.0, 2.0, and 3.0‰), mean results for f_{ox} are shown for the combined Proterozoic data (filled red circles) and combined Phanerozoic data (filled black circles). Error bars show ±1σ for the estimated f_{ox} values of the entire subsampled dataset. Given that positive δ^{56}Fe values can only be explained by low [O_2], yet a range of lower δ^{56}Fe values are expected in this scenario, minimum f_{ox} estimates based upon the degree of fractionation within a sample set are relevant to estimating background [O_2] levels. Therefore, we also calculate a range of minimum f_{ox} estimates by filtering Proterozoic data to exclude nonfractionated samples relative to the range of likely input values ($-0.5 < \delta^{56}Fe < 0.3$‰; open red circles). Shown in *B* are results for f_{ox} estimated from a kinetic model of Fe(II) oxidation, resampled 10,000 times at each atmospheric pO_2 value (relative to PAL), across a range of seawater pH and temperature values (*SI Appendix*). Error bars show ±1σ. The corresponding surface seawater [O_2] values at each atmospheric pO_2 value, assuming gas-exchange equilibrium (42), are shown in blue. The systematics of the observed Proterozoic samples are difficult to explain unless atmospheric pO_2 was below ~1% PAL, while Phanerozoic data imply a minimum atmospheric pO_2 of ~5% PAL.

Ironstone samples with δ^{56}Fe values that fall within the range of igneous and hydrothermal Fe(II) sources could be consistent with quantitative Fe(II) oxidation. For ironstone samples that are fractionated beyond the relatively narrow range of δ^{56}Fe values of possible input values, we can use a distillation model to invert each ironstone δ^{56}Fe value and estimate the fraction of the Fe(II) reservoir that was oxidized (f_{ox}; Fig. 4*A* and *SI Appendix*). This process is repeated using different values for the assumed combined isotope fractionation effect for Fe(II) oxidation and precipitation in shallow seawater. Following this, we can compare these results for the extent of Fe(II) oxidation to those obtained using a probabilistic model of Fe(II) oxidation kinetics that takes into account a wide range of possible marine pH values, surface water temperatures, and variable residence times of water masses within the shallow ocean (Table 1 and *SI Appendix*, Fig. S1). We run this model at a range of seawater [O_2] and utilize the results from a Lagrangian model embedded within a general circulation model (12) to approximate a surface water residence time. This produces a statistical distribution of the values for f_{ox} obtained for each δ^{56}Fe data point; these results are shown in Fig. 4. Based on the results of this modeling approach, we find that the signatures observed in Proterozoic ironstones are most compatible with shallow seawater [O_2] below ~5 μmol/kg (Fig. 4*B*). At these low O_2 levels, some proportion of the Fe(II) oxidation is likely to have been mediated by microaerophilic chemotrophic bacteria, which would lead to isotopic fractionation similar to that of abiotic oxidation (18). Given that microbial rates of Fe(II) oxidation at low [O_2] are higher than abiotic oxidation rates (38), our [O_2] estimate of <5 μmol/kg is likely to be conservatively high. This is evident when comparing our model constraints to the much lower estimates for shallow water [O_2] that would be obtained using a dispersion–reaction modeling approach that has been used in other Fe isotope studies (14, 37). Such low surface water [O_2]—as indicated by the maximum constraints provided by our model—would be expected to have exerted a powerful control on the ecology of even the shallowest marine environments during this time (39, 40).

Table 1. Kinetic Fe oxidation model parameters

Parameter	Value
Mixed layer depth	
Upper	90 m
Lower	50 m
Mixed layer residence time	Lognormal distribution according to general circulation model (*SI Appendix*, ref. 12)
Seawater conditions	
pH	6.8–8.8
Temperature	15–35 °C
Ionic strength	0.7 M
Salinity	35‰
Atmospheric pO_2	0.1–10% PAL
Fe(II) input δ^{56}Fe	−0.5 to 0.3‰

Surface seawater [O_2] is linked to atmospheric pO_2 via air–sea gas exchange. The Fe(III) (oxyhydr)oxide precursor minerals of the studied ironstones were precipitated from shallow seawater (above storm wave base). In modern marine environments, such settings are well mixed and unlikely to be deficient in dissolved O_2 relative to equilibrium with the overlying oxygenated atmosphere, except in cases of extreme eutrophy (41). In the mid-Proterozoic, the flux of O_2 supplied by air–sea gas exchange at $pO_2 \geq 1\%$ of the present atmospheric level (PAL) is unlikely to have been exhausted by upwelling ferruginous seawater, given estimates of dissolved Fe(II) concentrations and assuming reasonable upwelling rates (*SI Appendix*, Fig. S2; calculations in *SI Appendix*). Therefore, the predominance of Fe isotopic evidence for low surface water [O_2] from ironstones, deposited in a range of paleocontinents and time periods in the mid-Proterozoic, is extremely difficult to explain unless atmospheric pO_2 was low during for at least intervals of the Proterozoic. Assuming gas-exchange equilibrium, with solubility corrections for temperature and salinity (42), our results strongly suggest that atmospheric pO_2 reached levels below 1% PAL (Fig. 4*B*), at least during the sampled intervals throughout the mid-Proterozoic. These results are supported by other geological evidence, such as mid-Proterozoic paleosols that suggest Fe loss during weathering, which is also consistent with a low-O_2 atmosphere (43). Regardless of whether low shallow water [O_2]

might have been toxic to the earliest animal life, low O_2 levels in the ocean–atmosphere system would have exerted an important limitation on marine nutrient levels, primary productivity, and the potential for oceans to sustain complex, eukaryote-rich ecosystems (44). As such, new, robust evidence for the presence of low surface O_2 levels bolsters the case that oxygenation may have played a significant role in constraining the structure and energetic scope of complex life in the Proterozoic biosphere (3, 45).

Late Proterozoic Oxygenation and the Rise of Eukaryotes

The hypothesis that there was a mechanistic link between a rise in atmospheric pO_2 and the emergence of animals toward the end of the Proterozoic (e.g., ref. 3) remains debated. Specifically, an O_2 control on eukaryote complexity has recently been challenged on the grounds that the O_2 requirements of primitive animals were exceeded well before their evolution (7–9). Much of the debate stems from uncertainties associated with the assumptions used in various paleoredox approaches to translate geochemical data from sedimentary rocks into O_2 estimates (5, 9, 10), leading to estimates that span over an order of magnitude (e.g., refs. 4, 5, 7, 8, 43).

For instance, the chromium (Cr) isotope proxy system has been used to argue for low atmospheric pO_2 (i.e., 0.1 to 1.0% PAL) (4, 46) as well as higher levels (>1 to 10% PAL) (7, 10). This proxy links the Cr isotope composition of marine sediments to atmospheric pO_2, whereby the oxidative weathering of terrestrial rocks supplies fractionated Cr to the marine realm (e.g., ref. 46). Nonredox-dependent and marine processes have also been shown to fractionate Cr, and the interpretation of atmospheric pO_2 based upon Cr isotope data may yield multiple, nonunique solutions (47, 48). Therefore, the Cr sedimentary isotope record tracks a complex history of Cr weathering, transport, and burial and compared to the Fe isotope proxy is less directly linked to the shallow seawater $[O_2]$ critical to eukaryotic evolution. Further, the Cr isotope pO_2 proxy relies on the preservation of a trace element which may be overprinted during diagenesis and alteration (49, 50). Another approach that has been used to estimate mid-Proterozoic paleoredox conditions involves the abundance of cerium (Ce) in marine carbonate rocks (5, 6, 12), as Ce is preferentially scavenged from seawater under oxic conditions (51). However, poorly constrained Ce oxidation kinetics and debate over the oxidative pathway (e.g., refs. 51 and 52) present a challenge for attempts to quantitatively link Ce anomaly records to O_2 levels, and different modeling approaches have led to discrepancies in estimates for mid-Proterozoic atmospheric pO_2 (5, 12).

In comparison, the kinetics of Fe(II) oxidation—and the associated Fe isotope systematics—are relatively well-constrained, building on the foundation of research spanning over two decades and summarized in recent literature reviews (17, 18). Our approach is based on a major element, and compared to some other proxies ironstone Fe isotope signals are more likely to be preserved during the postdepositional history of the rocks. Perhaps most importantly, many mid-Proterozoic redox proxy data come from sedimentary rocks deposited in comparatively deeper marine settings (such as shales). The ironstone Fe isotope proxy is more directly related to O_2 levels in shallow marine environments that hosted the evolution of early aerobic eukaryotes, and our kinetic model for Fe(II) oxidation is able to provide critical quantitative constraints on relevant shallow seawater $[O_2]$.

Geochemical evidence (largely from the shale record) has been used to argue for the oxygenation of the deep oceans in the late Proterozoic, possibly during the Ediacaran Period (635 to 541 Ma) (e.g., refs. 45 and 53). However, estimates for the timing of hypothesized late Proterozoic oxygenation span hundreds of millions of years, and the magnitude of this hypothesized rise in pO_2 lacks consensus, making it difficult to test hypotheses regarding the cause-and-effect relationships between oxygenation and eukaryotic evolution (e.g., see ref. 11). Our ironstone dataset suggests an earlier oxygenation event, which led to more O_2-rich shallow waters in the Tonian Period (1,000 to 720 Ma), as evidenced by positive $\delta^{56}Fe$ values in the *ca*. 900 Ma Nelson Head and McClure ironstones of Canada, yet negligible fractionation in the *ca*. 750 Ma Galeros Formation ironstone (Fig. 2). The absence of a correlation between $\delta^{56}Fe$ values and detrital proxies (*SI Appendix*, Fig. S6), and the similar petrography of the Galeros Formation ironstone to other Proterozoic ironstones, suggests that these observed trends are not driven by mineralogical controls or detrital contribution. To our knowledge, there are no other shallow-marine ironstones reported from the late Proterozoic; positive $\delta^{56}Fe$ values in iron formations associated with the *ca*. 720 Ma Snowball Earth event were deposited under ice cover in disequilibrium with the atmosphere (54) and were not considered in this study. Therefore, although they provide only a limited temporal snapshot, our new ironstone data suggest a change in surface O_2 levels in the Tonian Period and narrow down the timing of this oxygenation to between *ca*. 900 and 750 Ma (*SI Appendix* for geochronological details). This oxygenation is broadly coincident with independent evidence for redox-driven biogeochemical change during this interval, including the reorganization of the phosphate (55) and sulfate (e.g., ref. 56) cycles, as recorded by marine sedimentary rocks.

Implications for Global Oxygen Cycles and Eukaryotic Evolution

The ironstone record of low atmospheric pO_2 (less than ~1% PAL) during the mid-Proterozoic highlights gaps in our mechanistic understanding of the O_2 cycle, given that some models have questioned the stability of low-O_2 worlds (e.g., see ref. 57). This possibility suggests that following the Great Oxidation Event, atmospheric pO_2 was high enough to form an ozone layer that shielded near-surface O_2 from photolysis (58), yet the oxygen cycle included sufficient feedbacks that could maintain pO_2 below ~1% PAL. The subsequent oxygenation of surface environments toward the end of the Proterozoic also coincides with biomarker evidence for the rise of eukaryote-dominated ecosystems (59, 60) and an apparent rise in eukaryotic fossil diversity (61, 62). Evidence for drill holes and biomineralized scales in late Tonian fossils (63, 64) may indicate greater eukaryotic predation during this time. As the ingestion of larger cells is an O_2-intensive activity (61), and eukaryotic predation is thought to be near-absent in modern anoxic habitats (40), low marine $[O_2]$ may have restricted this behavior in earlier ecosystems. Further, redox-related nutrient limitations on primary productivity prior to the middle Tonian may have exerted a strong control on ecosystem structure and eukaryotic predation (44). A mid-to-late-Tonian oxygenation event could therefore have provided both the requisite O_2 and nutrient supply for the proliferation of eukaryotic predation via a concomitant reorganization of the phosphorus cycle (44). Some molecular clock analyses estimate that animals may have first diverged during this time (65) (Fig. 2*A*), and tentative fossil evidence for primitive metazoans (sponges) is reported from mid-Tonian strata (66). The selective pressure of expanded eukaryotic predation may have been a controlling factor in the timing of the emergence of animal multicellularity during this time (61, 62). Therefore, our evidence from the ironstone record provides critical support for the idea that surface O_2 levels were changing in step with eukaryotic evolution in the Proterozoic.

Materials and Methods

Ironstone samples were collected from surface outcrop and supplemented by samples from the University of Cincinnati Museum and the Yale Peabody Museum collections. These samples were prepared as polished thin sections

and analyzed using reflected light microscopy, Raman spectroscopy, and scanning electron microscopy. Well-preserved ironstone samples were crushed in an agate mill to a fine powder, and sample powders (n = 201) were digested for bulk rock geochemical analyses. Major and trace element compositions were determined using an inductively coupled plasma-mass spectrometer (ICP-MS). For Fe isotope analysis, Fe was purified from sample solutions using ion-exchange chromatography and measured using a multicollector ICP-MS. Refer to *SI Appendix* for detailed methods.

Data Availability. All study data are included in the article and/or supporting information. All samples used in this study will be archived in the Yale Peabody Museum upon publication of this work.

ACKNOWLEDGMENTS. We thank the First Nation of Na-Cho Nyak Dun for granting permission to carry out this research on their traditional territory. We also acknowledge X. F. Wu for technical support. This research was supported by grants from the Key Research Program of Frontier Sciences, Chinese Academy of Sciences (CAS) (ZDBS-LY-DQC037), the Key Research Program of the Institute of Geology and Geophysics, CAS (Grant IGGCAS-201905), National Natural Science Foundation of China (Grants 41872087 and 41890833), Youth Innovation Promotion Association, CAS, and China Scholarship Council to C.W.; Fonds de Recherche du Québec Nature et Technologies Postdoctoral Scholarship to M.A.L.; a European Research Council Starting Grant (OOID No. 755053) to I.H.; and the Astrobiology Institute and the Interdisciplinary Consortia for Astrobiology Research of NASA's Astrobiology Program to T.W.L. and N.J.P. We thank the handling editor and two reviewers for their constructive feedback.

1. J. Farquhar, A. Zerkle, A. Bekker, "Geologic and Geochemical Constraints on the Earth's Early Atmosphere" in *Treatise on Geochemistry*, H. Holland, K. Turekian, Eds. (Elsevier, 2014), vol. **8**, pp. 91–138.
2. T. W. Lyons, C. T. Reinhard, N. J. Planavsky, The rise of oxygen in Earth's early ocean and atmosphere. *Nature* **506**, 307–315 (2014).
3. J. Nursall, Oxygen as a prerequisite to the origin of the Metazoa. *Nature* **183**, 1170 (1959).
4. N. J. Planavsky *et al.*, Earth history. Low mid-Proterozoic atmospheric oxygen levels and the delayed rise of animals. *Science* **346**, 635–638 (2014).
5. X.-M. Liu *et al.*, A persistently low level of atmospheric oxygen in Earth's middle age. *Nat. Commun.* **12**, 351 (2021).
6. D. Tang, X. Shi, X. Wang, G. Jiang, Extremely low oxygen concentration in mid-Proterozoic shallow seawaters. *Precambrian Res.* **276**, 145–157 (2016).
7. D. E. Canfield *et al.*, Highly fractionated chromium isotopes in Mesoproterozoic-aged shales and atmospheric oxygen. *Nat. Commun.* **9**, 2871 (2018).
8. D. E. Canfield *et al.*, Petrographic carbon in ancient sediments constrains Proterozoic Era atmospheric oxygen levels. *Proc. Natl. Acad. Sci. U.S.A.* **118**, e2101544118 (2021).
9. S. Zhang *et al.*, Sufficient oxygen for animal respiration 1,400 million years ago. *Proc. Natl. Acad. Sci. U.S.A.* **113**, 1731–1736 (2016).
10. G. J. Gilleaudeau *et al.*, Oxygenation of the mid-Proterozoic atmosphere: Clues from chromium isotopes in carbonates. *Geochem. Perspect. Lett.* **2**, 178–187 (2016).
11. D. B. Cole *et al.*, On the co-evolution of surface oxygen levels and animals. *Geobiology* **18**, 260–281 (2020).
12. E. J. Bellefroid *et al.*, Constraints on Paleoproterozoic atmospheric oxygen levels. *Proc. Natl. Acad. Sci. U.S.A.* **115**, 8104–8109 (2018).
13. A. Kappler, C. Pasquero, K. O. Konhauser, D. K. Newman, Deposition of banded iron formations by anoxygenic phototrophic Fe (II)-oxidizing bacteria. *Geology* **33**, 865–868 (2005).
14. A. D. Czaja *et al.*, Biological Fe oxidation controlled deposition of banded iron formation in the ca. 3770 Ma Isua Supracrustal Belt (West Greenland). *Earth Planet. Sci. Lett.* **363**, 192–203 (2013).
15. O. J. Rouxel, A. Bekker, K. J. Edwards, Iron isotope constraints on the Archean and Paleoproterozoic ocean redox state. *Science* **307**, 1088–1091 (2005).
16. V. Busigny *et al.*, Iron isotopes in an Archean ocean analogue. *Geochim. Cosmochim. Acta* **133**, 443–462 (2014).
17. N. Dauphas, S. G. John, O. Rouxel, Iron isotope systematics. *Rev. Mineral. Geochem.* **82**, 415–510 (2017).
18. C. M. Johnson, B. L. Beard, S. Weyer, *Iron Geochemistry: An Isotopic Perspective* (Springer, 2020).
19. Y. Lin, D. Tang, X. Shi, X. Zhou, K. Huang, Shallow-marine ironstones formed by microaerophilic iron-oxidizing bacteria in terminal Paleoproterozoic. *Gondwana Res.* **76**, 1–18 (2019).
20. K. O. Konhauser *et al.*, Iron formations: A global record of Neoarchaean to Palaeoproterozoic environmental history. *Earth Sci. Rev.* **172**, 140–177 (2017).
21. J. Petránek, F. B. Van Houten, "Phanerozoic ooidal ironstones: Contribution to the International Geological Correlation Programme, Project 277-Phanerozoic Ooidal Ironstones" (Czech Geological Survey, 1997), vol. 7.
22. A. Garcia-Frank, S. Ureta, R. Mas, Iron-coated particles from condensed Aalenian–Bajocian deposits: Evolutionary model (Iberian Basin, Spain). *J. Sediment. Res.* **82**, 953–968 (2012).
23. B. R. Johnson *et al.*, Phosphorus burial in ferruginous SiO_2-rich Mesoproterozoic sediments. *Geology* **48**, 92–96 (2020).
24. U. Raye, P. K. Pufahl, T. K. Kyser, E. Ricard, E. E. Hiatt, The role of sedimentology, oceanography, and alteration on the δ56Fe value of the Sokoman Iron Formation, Labrador Trough, Canada. *Geochim. Cosmochim. Acta* **164**, 205–220 (2015).
25. Z. Li, X.-K. Zhu, Geochemical features of Xuanlong type iron ore deposit in Hebei Province and their geological significance. *Yanshi Xuebao* **28**, 2903–2911 (2012).
26. S. Todd, P. Pufahl, J. Murphy, K. Taylor, Sedimentology and oceanography of early Ordovician ironstone, Bell Island, Newfoundland: Ferruginous seawater and upwelling in the Rheic Ocean. *Sediment. Geol.* **379**, 1–15 (2019).
27. R. Aller, J. Mackin, R. Cox Jr., Diagenesis of Fe and S in Amazon inner shelf muds: Apparent dominance of Fe reduction and implications for the genesis of ironstones. *Cont. Shelf Res.* **6**, 263–289 (1986).
28. S. Severmann, T. W. Lyons, A. Anbar, J. McManus, G. Gordon, Modern iron isotope perspective on the benthic iron shuttle and the redox evolution of ancient oceans. *Geology* **36**, 487–490 (2008).
29. F. Kurzweil, M. Wille, N. Gantert, N. J. Beukes, R. Schoenberg, Manganese oxide shuttling in pre-GOE oceans—Evidence from molybdenum and iron isotopes. *Earth Planet. Sci. Lett.* **452**, 69–78 (2016).
30. C. T. Reinhard, N. J. Planavsky, S. L. Olson, T. W. Lyons, D. H. Erwin, Earth's oxygen cycle and the evolution of animal life. *Proc. Natl. Acad. Sci. U.S.A.* **113**, 8933–8938 (2016).
31. M. Labatut *et al.*, Iron sources and dissolved-particulate interactions in the seawater of the Western Equatorial Pacific, iron isotope perspectives. *Global Biogeochem. Cycles* **28**, 1044–1065 (2014).
32. K. Dideriksen, J. A. Baker, S. L. S. Stipp, Equilibrium Fe isotope fractionation between inorganic aqueous Fe (III) and the siderophore complex, Fe (III)-desferrioxamine B. *Earth Planet. Sci. Lett.* **269**, 280–290 (2008).
33. F. Scholz *et al.*, On the isotope composition of reactive iron in marine sediments: Redox shuttle versus early diagenesis. *Chem. Geol.* **389**, 48–59 (2014).
34. F. Poitrasson *et al.*, Iron isotope composition of the bulk waters and sediments from the Amazon River Basin. *Chem. Geol.* **377**, 1–11 (2014).
35. R. Guilbaud, I. B. Butler, R. M. Ellam, Abiotic pyrite formation produces a large Fe isotope fractionation. *Science* **332**, 1548–1551 (2011).
36. J. M. Rolison *et al.*, Iron isotope fractionation during pyrite formation in a sulfidic Precambrian ocean analogue. *Earth Planet. Sci. Lett.* **488**, 1–13 (2018).
37. A. W. Heard *et al.*, Triple iron isotope constraints on the role of ocean iron sinks in early atmospheric oxygenation. *Science* **370**, 446–449 (2020).
38. C. S. Chan, D. Emerson, G. W. Luther III, The role of microaerophilic Fe-oxidizing micro-organisms in producing banded iron formations. *Geobiology* **14**, 509–528 (2016).
39. V. P. Edgcomb, Marine protist associations and environmental impacts across trophic levels in the twilight zone and below. *Curr. Opin. Microbiol.* **31**, 169–175 (2016).
40. T. Fenchel, "Anaerobic Eukaryotes" in *Anoxia: Evidence for Eukaryote Survival and Paleontological Strategies*, A. V. Altenbach, J. M. Bernhard, J. Seckbach, Eds. (Springer Netherlands, Dordrecht, 2012), pp. 3–16.
41. N. Rabalais *et al.*, Dynamics and distribution of natural and human-caused hypoxia. *Biogeosciences* **7**, 585–619 (2010).
42. H. E. Garcia, L. I. Gordon, Oxygen solubility in seawater: Better fitting equations. *Limnol. Oceanogr.* **37**, 1307–1312 (1992).
43. N. J. Planavsky *et al.*, A case for low atmospheric oxygen levels during Earth's middle history. *Emerg. Top. Life Sci.* **2**, 149–159 (2018).
44. C. T. Reinhard *et al.*, The impact of marine nutrient abundance on early eukaryotic ecosystems. *Geobiology* **18**, 139–151 (2020).
45. D. E. Canfield, S. W. Poulton, G. M. Narbonne, Late-Neoproterozoic deep-ocean oxygenation and the rise of animal life. *Science* **315**, 92–95 (2007).
46. D. B. Cole *et al.*, A shale-hosted Cr isotope record of low atmospheric oxygen during the Proterozoic. *Geology* **44**, 555–558 (2016).
47. E. M. Saad, X. Wang, N. J. Planavsky, C. T. Reinhard, Y. Tang, Redox-independent chromium isotope fractionation induced by ligand-promoted dissolution. *Nat. Commun.* **8**, 1590 (2017).
48. M. Miletto *et al.*, Marine microbial Mn (II) oxidation mediates Cr (III) oxidation and isotope fractionation. *Geochim. Cosmochim. Acta* **297**, 101–119 (2021).
49. C. Wang *et al.*, Chromium isotope systematics and the diagenesis of marine carbonates. *Earth Planet. Sci. Lett.* **562**, 116824 (2021).
50. A. B. Frank, R. M. Klaebe, S. Löhr, L. Xu, R. Frei, Chromium isotope composition of organic-rich marine sediments and their mineral phases and implications for using black shales as a paleoredox archive. *Geochim. Cosmochim. Acta* **270**, 338–359 (2020).
51. M. Bau, A. Koschinsky, Oxidative scavenging of cerium on hydrous Fe oxide: Evidence from the distribution of rare earth elements and yttrium between Fe oxides and Mn oxides in hydrogenetic ferromanganese crusts. *Geochem. J.* **43**, 37–47 (2009).
52. J. W. Moffett, The relationship between cerium and manganese oxidation in the marine environment. *Limnol. Oceanogr.* **39**, 1309–1318 (1994).
53. L. M. Och, G. A. Shields-Zhou, The Neoproterozoic oxygenation event: Environmental perturbations and biogeochemical cycling. *Earth Sci. Rev.* **110**, 26–57 (2012).
54. M. A. Lechte *et al.*, Subglacial meltwater supported aerobic marine habitats during Snowball Earth. *Proc. Natl. Acad. Sci. U.S.A.* **116**, 25478–25483 (2019).
55. C. T. Reinhard *et al.*, Evolution of the global phosphorus cycle. *Nature* **541**, 386–389 (2017).

56. J. K. Prince, R. H. Rainbird, B. A. Wing, Evaporite deposition in the mid-Neoproterozoic as a driver for changes in seawater chemistry and the biogeochemical cycle of sulfur. *Geology* **47**, 375–379 (2019).
57. S. J. Daines, B. J. Mills, T. M. Lenton, Atmospheric oxygen regulation at low Proterozoic levels by incomplete oxidative weathering of sedimentary organic carbon. *Nat. Commun.* **8**, 14379 (2017).
58. C. Goldblatt, T. M. Lenton, A. J. Watson, Bistability of atmospheric oxygen and the Great Oxidation. *Nature* **443**, 683–686 (2006).
59. J. A. Zumberge, D. Rocher, G. D. Love, Free and kerogen-bound biomarkers from late Tonian sedimentary rocks record abundant eukaryotes in mid-Neoproterozoic marine communities. *Geobiology* **18**, 326–347 (2019).
60. J. J. Brocks *et al.*, Early sponges and toxic protists: Possible sources of cryostane, an age diagnostic biomarker antedating Sturtian Snowball Earth. *Geobiology* **14**, 129–149 (2016).
61. A. H. Knoll, D. Lahr, "Fossils, feeding, and the evolution of complex multicellularity" in *Multicellularity: Origins and Evolution*, K. J. Niklas, S. A. Newman, Eds. (*Vienna Series in Theoretical Biology*, MIT Press, Boston, 2016), pp. 3–16.
62. A. H. Knoll, Paleobiological perspectives on early eukaryotic evolution. *Cold Spring Harb. Perspect. Biol.* **6**, a016121 (2014).
63. S. M. Porter, Tiny vampires in ancient seas: Evidence for predation via perforation in fossils from the 780-740 million-year-old Chuar Group, Grand Canyon, USA. *Proc. Biol. Sci.* **283**, 20160221 (2016).
64. P. A. Cohen, J. V. Strauss, A. D. Rooney, M. Sharma, N. Tosca, Controlled hydroxyapatite biomineralization in an ~810 million-year-old unicellular eukaryote. *Sci. Adv.* **3**, e1700095 (2017).
65. M. dos Reis *et al.*, Uncertainty in the timing of origin of animals and the limits of precision in molecular timescales. *Curr. Biol.* **25**, 2939–2950 (2015).
66. E. C. Turner, Possible poriferan body fossils in early Neoproterozoic microbial reefs. *Nature* **596**, 87–91 (2021).
67. C. C. Loron, R. H. Rainbird, E. C. Turner, J. W. Greenman, E. J. Javaux, Implications of selective predation on the macroevolution of eukaryotes: Evidence from Arctic Canada. *Emerg. Top. Life Sci.* **2**, 247–255 (2018).
68. A. W. Heard, N. Dauphas, Constraints on the coevolution of oxic and sulfidic ocean iron sinks from Archean–Paleoproterozoic iron isotope records. *Geology* **48**, 358–362 (2020).